

Final Technical Report

External Grant Award Number: G14AP00056

Title: Nonvolcanic Tremor and Shear Wave Velocity Structure of the Crust
in the Parkfield Region

Author and Affiliation: Clifford Thurber
University of Wisconsin-Madison
1215 W. Dayton St.
Madison, WI 53706
Phone: (608) 262-6027, FAX: (608) 262-0693
clifft@geology.wisc.edu

Term covered by the award: May 1, 2014 - December 31, 2015

Nonvolcanic Tremor and Shear Wave Velocity Structure of the Crust in the Parkfield Region

Abstract

Although our UW-Madison research group and our collaborators have previously had excellent success in developing three-dimensional (3D) P-wave velocity (V_p) models of the crust of California at regional scales using body-wave tomography (Thurber et al., 2006; Thurber et al., 2007; Thurber et al., 2009; Lin et al., 2010), comparable large-scale models for 3D S-wave velocity (V_s) and/or V_p/V_s with similar, useful resolution have only been developed for a few regions. In this project, we develop a V_s model for the greater Parkfield region (essentially the area studied by Thurber et al. (2006)), and extend the resolved volume of both the V_p and V_s models to greater depth using data from low-frequency earthquakes (LFEs). We also investigated the effect of different processing and location techniques used for LFEs versus nonvolcanic tremor (NVT) to assess the potential for location bias in one approach versus the other. In parallel, we have begun to investigate surface-wave dispersion in the region from ambient noise. This project has capitalized on previous results and new efforts being carried out with support from NSF and SCEC, thus substantially leveraging resources.

There are three main underlying goals of the proposed project. One is to develop a 3D regional-scale V_s model that can be used for determining improved earthquake locations and for carrying out waveform modeling and geodetic calculations. For example, strong motion modeling of the 2004 Parkfield earthquake can be done more accurately if a 3D V_s model is available, a reasonable 3D V_s model can be a starting point for spectral element waveform inversion, and a 3D model of elastic moduli derived from V_p and V_s can be used for finite-element modeling of geodetic data covering the Parkfield earthquake cycle. The second is to extend the existing V_p model and develop new V_s and V_p/V_s models to cover the depth range of the NVT that is present beneath the San Andreas fault (SAF) in the region around Parkfield. The reason that ambient and triggered NVT is present beneath this area has mainly been attributed to the presence of fluids (Ghosh et al., 2009; Peng et al., 2008, 2009; Nadeau and Guilhem, 2009; Thomas et al., 2009, 2012; Hill and Prejean, 2013). The velocity models will help constrain the lithologies and conditions present in the NVT zone. We initially used arrival time data from stacked LFEs beneath the temporary PASO array that was centered around SAFOD to endeavor to extend our tomographic model to greater depth. We expanded our use of LFEs using data from additional sources, including both permanent network and temporary array stations. Our third goal is to locate all well-recorded LFE families in the region as part of a joint inversion for location and 3D structure including the data from multiple networks and arrays. Previous studies have yielded different results for the depths of LFEs versus NVT, their degree of spatial clustering, and their locations relative to the SAF. These differing results lead to different conclusions about the origin and nature of SAF NVT and LFEs. We also investigated the effect of the processing and location methods used for LFEs compared to NVT to see if there is a possible source of bias in one approach versus the other. We believe that our unified approach yields the most robust results possible for the locations of the LFEs, thereby leading to a more confident interpretation for the genesis of LFEs and NVT and the implications for fluids beneath the SAF.

This project addresses two of the basic priorities under the Earthquake Physics and Occurrence element: "Develop and test models of fault zone structure and physical properties, such as fault strength, fault zone damage, porosity, permeability, post-seismic changes in properties, and of earthquake occurrence near Parkfield, in central California, and elsewhere using monitoring data, laboratory measurements on fault samples, crustal property observations, fault zone guided waves, borehole seismic networks, and other geophysical techniques," and "Conduct field and laboratory studies to ascertain the mechanisms (e.g., fluid flow or fault rheology) responsible for episodic tremor and slip (ETS) as observed in subduction zones, on the San Andreas Fault or in other tectonic settings." In particular, our work probes the structure of the SAF, using LFEs, in the depth range where there is evidence for precursory slip prior to the 2004 Parkfield earthquake (Shelly, 2009). We also examine the degree of localization of the zone of shear in which the LFEs occur, which has implications for the potential for seismic ruptures to penetrate into the deeper parts of the SAF. These results in turn can provide input for hazard estimation and may contribute to providing a new avenue for earthquake warning.

Report

This report is separated into three parts: (1) Parkfield region tomography including LFEs, (2) preliminary surface-wave dispersion analysis in the greater Parkfield region from ambient noise, and (3) LFE and NVT location.

(1) Parkfield region tomography including LFEs

The SAF at Parkfield and the surrounding region of central California have been the subject of intensive geophysical and geological investigation for the last few decades. One initial phase of emphasis was due to the Parkfield Prediction Experiment (PPE). Bakun and Lindh (1985) predicted a time window of 1988 ± 5 years for a recurrence of the Parkfield M 6 earthquake, leading to a major, sustained geophysical monitoring effort. Although the prediction itself was not successful, the substantial knowledge resulting from the PPE played a role in the selection of the Parkfield segment of the SAF for a major fault-zone drilling project, the San Andreas Fault Observatory at Depth (SAFOD). Planning for SAFOD in turn led to renewed geological and geophysical investigations, particularly at finer scales. The occurrence of the Parkfield earthquake in September 2004, after the completion of Phase II of the SAFOD drilling, refocused some attention on the larger scale structure around Parkfield, including the modeling of strong motion and geodetic data for the 2004 earthquake.

Thurber et al. (2006) developed a regional 3D P-wave velocity model for the greater Parkfield region, and used it to relocate thousands of earthquakes and determine focal mechanisms for about 450 earthquakes. Their model has since been used to estimate 3D S-wave velocity models, using empirical relations, for locating LFEs (Shelly and Hardebeck, 2010) and determining 3D Green's functions for strong motion modeling (Gallovic et al. 2010; Şeşetyan et al., 2015). Here we extend the 3D tomography work of Thurber et al. (2006) to produce a 3D S-wave velocity model and an improved P-wave velocity model by substantially increasing the number of earthquakes in the dataset, vastly enlarging the available S picks using a new automatic picker (Rawles and Thurber, 2015), and incorporating picks from stacks of LFE families computed with phase-weighted stacking (Thurber et al., 2014). The inclusion of LFE data also allows us to extend the depth of imaging to the lower crust where the LFEs occur.

Our results image not only previously identified features but also low velocity zones (LVZs) in the area around the LFEs and in the lower crust beneath the southern Rinconada fault. The former LVZ is consistent with high fluid pressure that can account for several aspects of LFE behavior. The latter LVZ is consistent with a high conductivity zone detected in magnetotelluric studies. A new V_s model was developed with S picks that were obtained with a new auto-picker. At shallow depth, low V_s zones underlie the areas of strongest shaking in the 2004 Parkfield earthquake. A high V_p/V_s zone in the middle crust on the northwest side of the San Andreas Fault was also revealed. We relocate LFE families and analyze their location uncertainties with the NonLinLoc and tomoDD algorithms. The two methods yield similar results.

Data and Method

The starting point for our dataset is that of Thurber et al. (2006). The previous dataset includes 80,823 picks at 923 stations from 2,374 events. We extended that with data from several sources. More than 11,000 P and S picks at the PG&E Central Coast Seismic Network were added. To better constrain S-wave structure, a new S-wave autopicker (Rawles and Thurber, 2015) was employed to pick S arrivals at Northern California Seismic Network stations as well as at the PERMIT array (Parkfield Experiment to Record Microseismicity and Tremor; Horstmann et al., 2013, 2015), which was deployed from May 2010 to June 2011. This picker provided 8,867 high quality S-wave picks from 151 earthquakes and 81 quarry blasts (as identified in the USGS catalog) to complement existing catalog P and S picks. The locations of quarry sites were identified using Google Earth. In total, 74 blasts have been assigned to four quarry sites. Both P and S arrivals from the LFE families have been previously picked at permanent stations (Shelly and Hardebeck, 2010). Additional picks at two temporary arrays, PASO (Parkfield Area Seismic Observatory; Thurber et al., 2003) and PERMIT, were obtained from stacks created with the tf-PWS stacking method (Thurber et al., 2014). Since picking is affected by signal quality, the original picks of

LFE data were checked by a quality control scheme based on differential time. We calculated the mean and standard deviation of differential times between event pairs, and the picks that were beyond two standard deviations were defined as outliers. We also measured differential times using cross-correlation at PASO stations to improve precision. Our final dataset includes 1,765 P and 2,949 S absolute arrivals from 87 LFE families. In total, there are 141,234 cross-correlation differential times, 850,939 catalog differential times, and 142,550 P and 26,447 S absolute times from 4,339 events.

With the differential and absolute times, hypocenters and 3D P- and S-wave velocity structure were jointly inverted with the tomoDD algorithm (Zhang and Thurber, 2003, 2006). Our starting model is based on Thurber et al. (2006) with additional horizontal nodes at $X = -25$ km and $Y = -40$ km (Figure 1). The nodes in the Z direction are at 0, 2, 4, 6, 9, 12, 16, 22, and 28 km. Nodes in the Y direction were modified to -70, -50, -40, -30, -21, -15, -9, -3, 9, 15, 21, 30, 40 and 50 km. Since the Vp/Vs model also shows strong lateral heterogeneity (Zhang et al., 2009), the Vp/Vs ratios at shallow depths (< 10 km) are set to be different on each side of the SAF in the upper crust of the starting model to reflect geologic differences. On the northeast side, the Vp/Vs ratio ranges from 1.9 near the surface to 1.72 at depth, whereas it ranges from 1.8 to 1.75 on the southwest side. The Vp/Vs ratio in the lower crust on both sides is computed with an empirical relationship (Brocher, 2005). There are still far fewer S than P picks, so a coarser mesh was introduced to invert the Vs model. Since the hypocenter relocation converges more slowly than inversion for velocity, we added a relocation step after each joint inversion step. The weight assigned to absolute arrivals is highest for early iterations, with the weight of differential times increased in subsequent iterations. The tomoDD code utilizes both damping and smoothing. The purpose of the damping parameter is to maintain an acceptable condition number for LSQR, although it also provides some regularization in the form of damping the amplitude of model perturbations. The smoothing is specifically for regularizing the roughness of the model perturbations. The smoothing constraints and damping factors were set according to a tradeoff curve analysis balancing data misfit and the norm of model perturbations. Both the smoothing constraints in three directions and the damping factor were kept constant during the inversion, at 20 and 45 respectively.

To test the quality of our results, we carried out standard checkerboard tests using the same data distribution and inversion parameters. The 1×1 checkerboards for very shallow depths ($Z = 1, 2$ km) could be recovered near the SAFOD site. The Vp structure between 4 km and 12 km depth could be well constrained by the substantial number of earthquakes that occur in the upper crust. The 2×2 Vs checkerboard at shallow depth ($Z = 0, 3$ km) could be recovered near the active fault zones and in the coastal area. In most areas, the Vs pattern can be recognized down to 21 km. As a result of the LFE data, the deepest checkers near the SAF fault zone could be recovered as well (Figure 2).

For the real data after 12 iterations, the root mean square residual (RMS) of both catalog and cross-correlation times were substantially reduced (Figure 3). The RMS of catalog times decreased about 57% (from 229 ms to 99 ms) whereas the RMS of cross-correlation times was reduced by about 66% (from 83.5 ms to 28.2 ms).

Inversion Results: Vp and Vs models

The velocity contrast across the SAF has been reported in previous 3D tomography models and reflection profiles (Michellini and McEvilly, 1991; Eberhart-Phillips and Michael, 1993; Thurber et al., 2006; Bleibinhaus et al., 2007; Roux, 2009). The southwest side is generally faster, corresponding to the granitic rocks of the Salinian block, whereas the northeast side with lower wave velocities consists mainly of the Great Valley sequence and Franciscan assemblage rocks. In the northern segment, the fault zone is dominated by a simple contrast across the fault (Figure 4; Y nodes from -3 to 30 km) that extends down to ~ 15 km depth in the Vp model. Due to resolution limitations, the Vs contrast across the SAF is smoother than that of the Vp model. Southwest of the SAF, a middle crust low velocity zone dipping to the southwest is clearly imaged in sections $Y = 9$ and 3 km of the Vs model (Figure 5). In the southern segment, the Vp and Vs model patterns across the SAF are similar to each other.

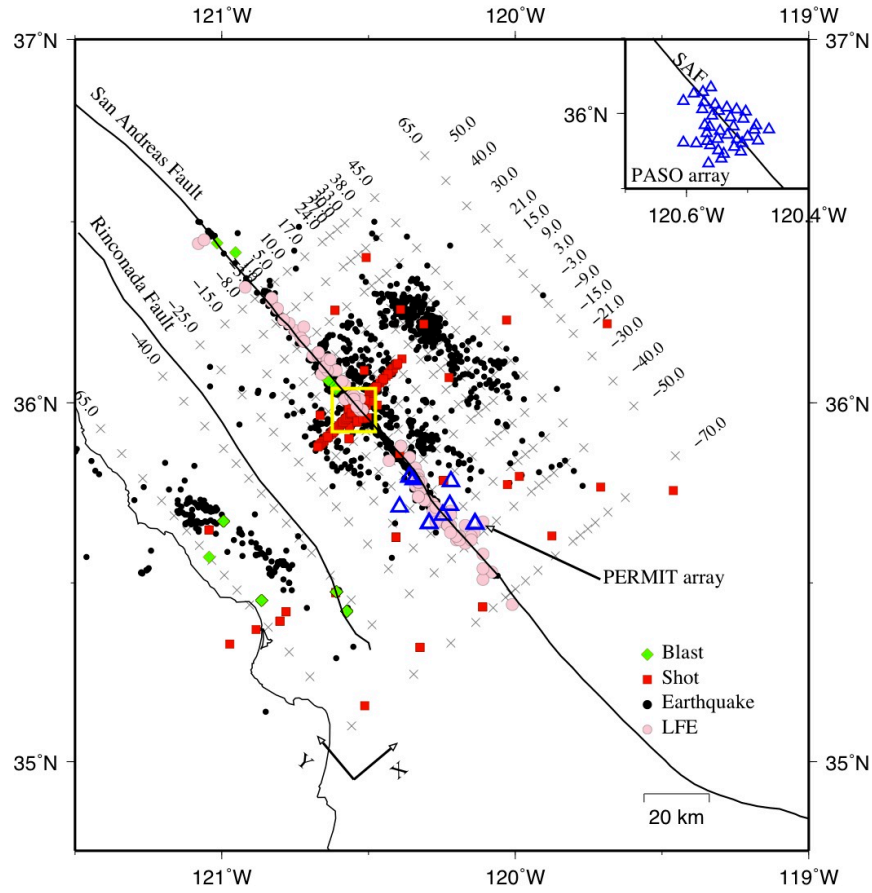


Figure 1. Map of the study area showing events (diamonds, squares, solid circles), two temporary arrays (open triangles, with the PASO array indicated by the yellow box and shown in the inset) and inversion grid (crosses). Shots, blasts earthquakes and LFEs are denoted by green, red, black, and pink symbols, respectively.

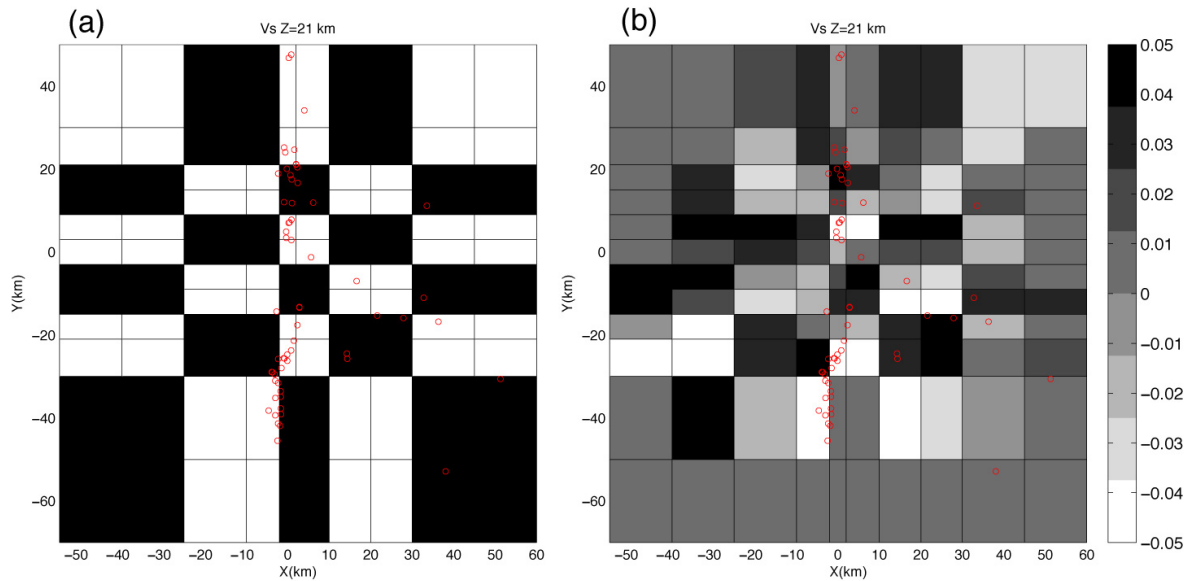


Figure 2. 2x2 checkerboard test result for the coarser mesh for the Vs model at 21 km depth. (a) Input model. (b) Output model. The red circles indicate events.

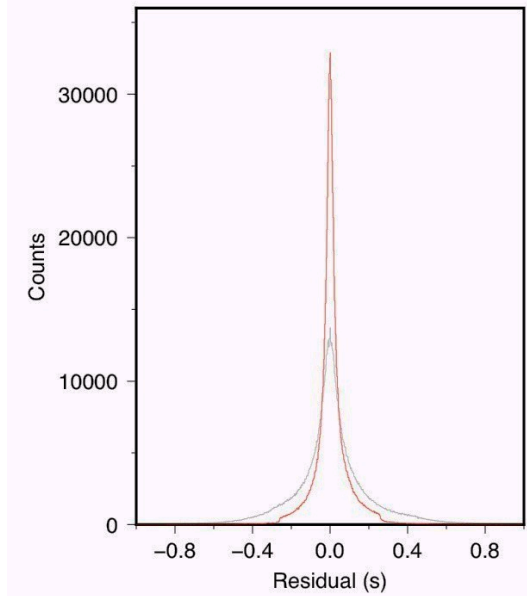


Figure 3. Histogram of arrival-time residuals before (gray) versus after (red) inversion.

We observed no clear velocity contrast across the Rinconada fault (about $X = -40$ km; Figures 4 and 5). Based on the velocities observed, the material on both sides of the Rinconada Fault likely belongs to the Salinian block. Previous large- and small-scale models suggested that there is no significant lateral variation in the upper crust near the Rinconada fault (Lin et al., 2010; Hardebeck, 2010).

A clear velocity contrast between the sedimentary rocks and underlying basement in the Coalinga area is obvious in sections from $Y = -3$ km to 50 km (down to about 10 km, Figure 4). In the V_p model, the high velocity body (HVB, $V_p \sim 6.0$ km/s) in the footwall is clearly visible from 12 km to 4 km depth and the southern part ($Y = 9$ km, Figure 4) is more sharply defined than the northern part. This feature has been interpreted as a fragment of the Coast Range Ophiolite sandwiched between the Franciscan and Great Valley sequence (Eberhart-Phillips, 1990). Since the V_s increase is much smaller in this HVB (Figure 5), the fault plane shows a strong contrast in V_p/V_s , which is consistent with expectations based on rock types (Brocher, 2005). The hanging wall appears as a LVZ ($Z = 9$ km, Figure 6b) that is likely an additional Great Valley sequence layer over basement. Although the main fault plane dips to the northeast, there is another possible southwest-dipping fault plane associated with a small earthquake cluster (dashed lines in Figure 4).

A small HVB on the southeast side of the SAF beneath Middle Mountain is also revealed at 4 km depth in the V_p model ($Y \sim -20$ to 0 km, Figure 6a; Eberhart-Phillips and Michael, 1993). In the V_s model, this HVB is present between 3 and 6 km depth, but appears somewhat smaller. This HVB is consistent with the existence of an elliptical magnetic and high gravity zone that was interpreted as magnetic granitic rocks over Salinian basement (McPhee et al., 2004).

A significant high velocity body on the northeast side of the SAF is imaged near Gold Hill that extends down to 10 km in the V_p model ($X \sim 1$ to 10 km, Figure 6b). This HVB was previously revealed in first-P-arrival tomography (Eberhart-Phillips and Michael, 1993; Thurber et al., 2006) and also confirmed with a dataset including secondary P arrivals (Bennington et al., 2013). In the V_s model, the HVB is not clear and the V_p/V_s ratio is significantly higher than the surrounding region. This region is marked by a 10 mGal isostatic residual gravity anomaly, indicating higher density rock (Synder and Carr, 1984). The velocity is even higher than that on the southwest side of the SAF, and it has been interpreted as greenstones and mafic rocks of the Permanente Terrain (Eberhart-Phillips and Michael, 1993; Thurber et al., 2006). The area corresponds approximately to the main rupture patch of the 2004 Parkfield mainshock. The high velocities on both sides of the fault suggest greater fault strength and the ability to store more strain energy to eventually release as a larger earthquake (Eberhart-Phillips and Michael, 1993; Thurber et al., 2006).

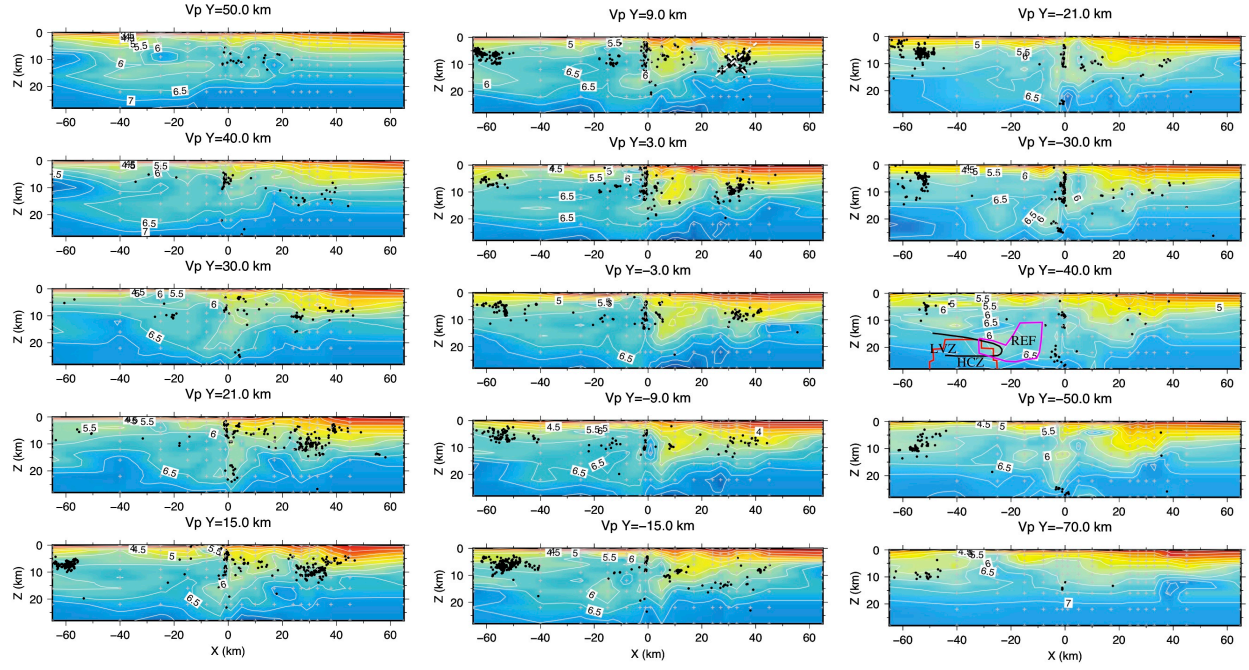


Figure 4. Cross-sections of the 3D Vp model. Earthquakes and LFE families are shown as black solid circles. Two potential fault planes in the Coalinga region are shown as dashed lines in the $Y = 9$ km cross-section. The LVZ (black; Trehu and Wheeler, 1987), the strong reflectivity zone (pink; Trehu and Wheeler, 1987), and HCZ (red; Becken et al., 2011) in previous results are shown in solid lines in the $Y = -40$ km cross-section. Vp in km/s.

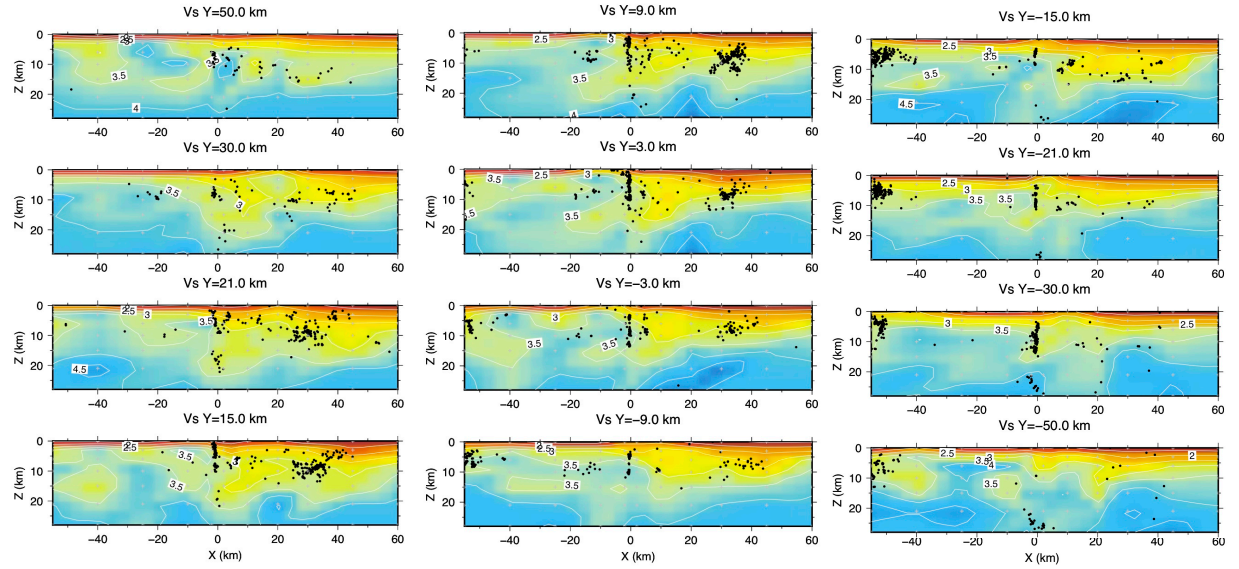


Figure 5. Cross-sections of the 3D Vs model. Earthquakes and LFE families are shown as black solid circles. Since a coarser mesh was adopted for the Vs model, the event locations are different than the ones in Figure 4. Vs in km/s.

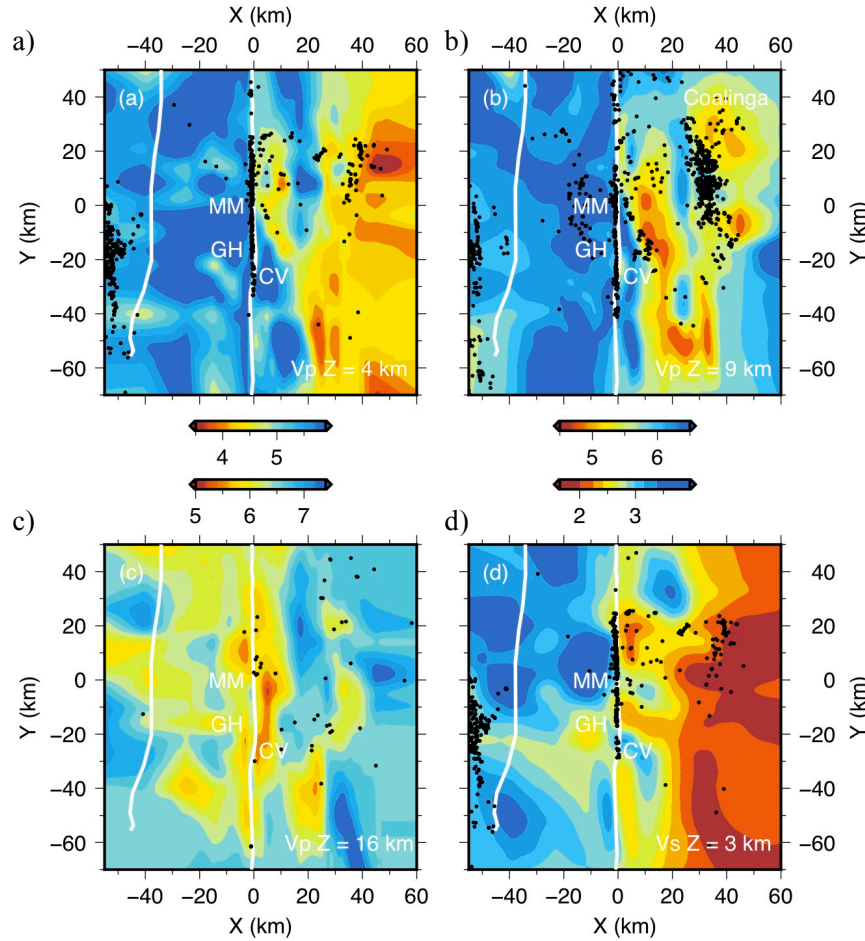


Figure 6. Map views of the (a-c) Vp and (d) Vs models (Vp at Z = 4 km, 9 km, 16 km, Vs at Z = 3 km). The surface traces of the SAF and Rinconada fault are shown by white line whereas black dots indicate events at depth. Local features: MM, Middle Mountain; GH: Gold Hills; CV: Cholame Valley and Coalinga: Coalinga area. Velocity in km/s.

At greater depth (Z = 9 km), this HVB connects with an along-strike linear HVB (Y = -21 to -50 km) that is about 2 km away from the SAF. The low velocity along the SAF trace may due to a broad damage zone with distributed parallel faults instead of a single fault in the upper crust, consistent with magnetic and gravity observations (Thurber et al., 2006).

Several other low velocity features are revealed in our results. Dimensions of the large low velocity basin-like feature on the northeast side of the SAF at 4 km depth are similar to previous results (X = 2 to 10 km, Y = 3 to 21 km; Eberhart-Phillips and Michael, 1993) with about a 10% Vp decrease. This LVZ is slightly larger and stronger in the Vs model. In gravity and aeromagnetic maps, this region is shown as an elliptical magnetic high and gravity low interpreted as serpentinite in Franciscan rocks (McPhee et al., 2004). This low velocity body also underlies the area of strongest shaking during the 2004 Parkfield mainshock (Bakun and Lindh, 2005). Besides the amplification effect of rupture directivity, the basin-like structure likely amplifies and extends the duration of ground motion (Gallovcic et al., 2010). Two other areas of low velocity at shallow depth are imaged in our Vs model (Figure 6d). The southeast one (X = -10 km, Y = -21 km) is close to the epicenter of the 2004 Parkfield earthquake. The other one (X = 2 km, Y = -30 to -50 km) is on the northeast side of the SAF near Cholame Valley. Both zones also underlie regions of strong ground shaking during the 2004 Parkfield mainshock (Bakun and Lindh, 2005; Shakal et al., 2006). The GH3W station in the southeast LVZ also recorded large ground motions during the 1983 Coalinga earthquake (Shakal et al., 2006). This consistency supports the influence of heterogeneity of shallow structure on ground motion (Gallovcic et al., 2010).

A lower crustal P-wave LVZ was imaged in the section Y = -40 km (Figure 4). Vp is reduced by about 0.5 km/s from the surrounding rock, but the LVZ is not clear in the Vs model. This LVZ is about 20

km by 20 km at 16 to 22 km depth and it may be in contact with the SAF. We note that the checkerboard pattern in this cross section was recovered adequately, suggesting we do have sufficient resolution to image these features (Figure 7). We also designed a restoration test to confirm our result. The test consists of a synthetic dataset that was generated from our final model. We then obtained an output model from an inversion of the synthetic dataset using the same parameters. The LVZ was recovered by the inversion (Figure 8). With reflection and refraction data, Trehu and Wheeler (1987) reported a LVZ (LVZ in Figure 4) in the lower crust between the SAF and Rinconada fault using reflection and refraction data collected along an active source profile located close to the $Y = -40$ km section. The depths of the two LVZs are comparable but our result is slightly east of that reported in Trehu and Wheeler (1987). In Trehu and Wheeler (1987), the LVZ location is consistent with the western portion of a strong reflectivity zone (REF in Figure 4), whereas the LVZ in our V_p model covers the eastern portion of the strong reflectivity zone. The slight difference could be due to sampling differences. The LVZ was sampled by deep reflected rays in Trehu and Wheeler (1987), which only sampled the western portion, whereas LFE data contributes most deep rays in the eastern portion in our inversion. Furthermore, an along strike high conductivity zone (HCZ) in the lower crust and upper-most mantle was imaged in a magnetotelluric inversion (HCZ in Figure 4; Becken et al., 2011) that is consistent with the presence of a LVZ. Becken et al. (2011) suggest that the lower crust is fluid rich and has been weakened. The slightly different locations for our LVZ and the high conductivity zone could again be due to different spatial sampling.

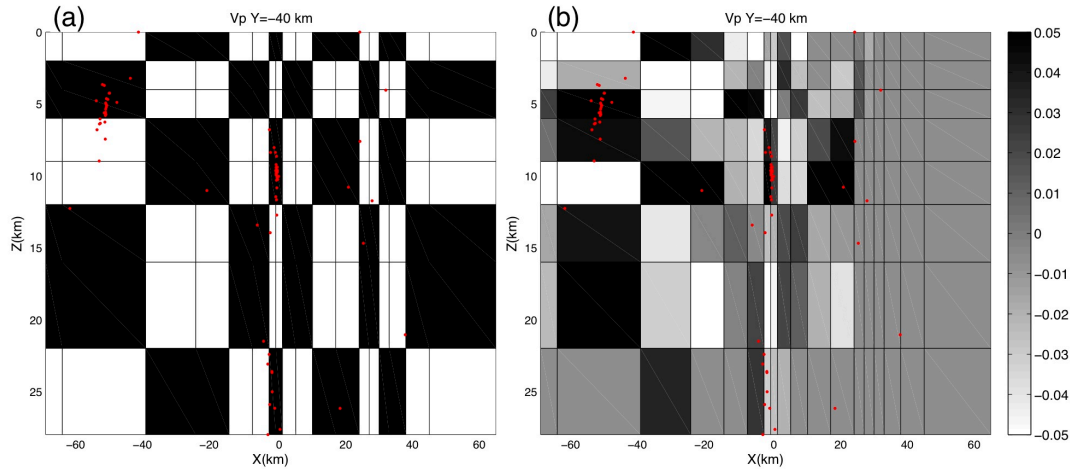


Figure 7. 2×2 checkerboard test result for the V_p model at $Y = -40$ km. The red dots indicate events.

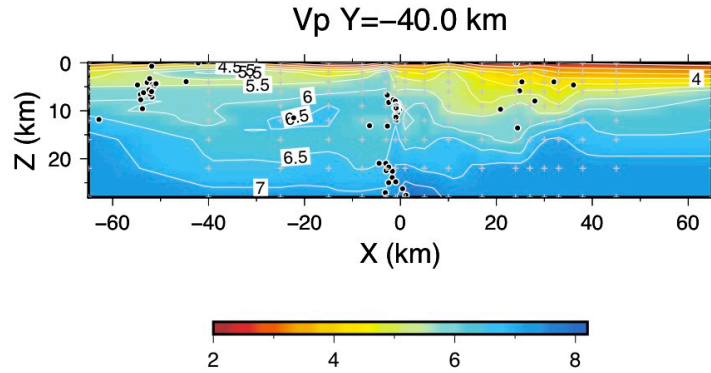


Figure 8. Cross section at $Y = -40$ km of the output model from the restoration test. The black dots indicate events. The LVZ in the lower crust on the southwest side of the SAF is recovered successfully.

There are two other LVZs in the deep crust ($Z = 16$ km, Figure 6c). One LVZ is close to the SAF to the north of Parkfield ($X = -8$ to 3 km, $Y = 15$ and 31 km). Another is to the east of Cholame ($X = 17$ km) where it is separated from the SAF by a narrow HVB. These LVZs in the lower crust may correspond to a low velocity layer in the receiver function study of Ozacar and Zandt (2009) that is interpreted to represent a layer of metasedimentary rocks.

Inversion Results: LFE locations

The locations of NVT have been studied with different datasets and location methods. In one approach, differential arrival times between station pairs measured with envelope cross-correlation were used with a grid search and station-pair double-difference location methods (Nadeau and Dolenc, 2005; Zhang et al., 2010). In a different approach, several small aperture arrays near Parkfield and Cholame provided high quality records that were used with array techniques to estimate the location of individual tremor events (Fletcher and Baker, 2010; Ryberg et al., 2010). In these studies, the location of NVT is generally widely scattered. In contrast to the generally emergent character of NVT wave trains, LFEs during tremor provide much clearer onsets of body waves, especially when LFE events with similar waveforms are stacked to improve signal quality (Shelly and Hardebeck, 2010). Using an a priori 3D Vs model to determine 88 LFE family locations, the results of the latter study suggest that most LFEs are concentrated close to the SAF trace at depths from 18 to 28 km, much shallower and more concentrated than the NVT results (Nadeau and Dolenc, 2005). However, the location difference between LFEs and NVT is still controversial (Shelly et al., 2009; Guilhem and Nadeau, 2012). Picks at temporary stations that are close to the SAF likely provide a tighter constraint on depth. Event-pair differential times can also be helpful to improve location precision.

In our results, the RMS misfits of most LFE families are less than 0.1 s and both horizontal and vertical uncertainties are less than 1 km (Figure 9). The uncertainties of LFE families in the northern segment are much larger than the southern ones. A grid search location method (Non-Linear Location, NonLinLoc; Lomax et al., 2009) was also utilized to evaluate the location results. The travel-time tables were calculated with our final velocity model using the finite difference algorithm. Although the NonLinLoc results are independent of the initial location, the final locations are very consistent with our result. This method also provides probability distribution functions of location that are a reliable estimate of uncertainties. As Figure 10 shows, the average length of the semi-major-axis of the 68% confidence ellipsoid is about 3 km. The location uncertainties for the southern LFEs are smaller than the northern ones due to a better station distribution, although the residuals are larger.

The overall pattern of our LFE relocations is consistent with the previous result of Shelly and Hardebeck (2010). The LFE families beneath Cholame Valley are concentrated in about a 4 km wide zone, about 3 km southwest of the surface trace of the SAF (Figure 9). There are some LFE families on the northeast side of the SAF separated from the clusters beneath the SAF. Shelly (2015) proposed that such isolated LFEs may occur along the upper interface of the Monterey microplate, a remnant of the subducted Farallon plate that might deflect the SAF eastward in the mantle. The LFE zone northwest of Parkfield is much wider in both horizontal and vertical directions in both the tomoDD and NonLinLoc results (Figures 9 and 10). Since the Y-direction uncertainties of the northern LFEs are obviously larger, the horizontal scatter of LFE families there may be caused by lower signal-to-noise ratio that reduces the precision of picking. The fault northwest of Parkfield is hypothesized to be much weaker due to presence of fluid (Becken et al., 2011) and the LFE amplitudes are about 50% lower than for ones beneath Cholame (Shelly and Hardebeck, 2010). A lower activity rate also limited the usable traces for stacking, that in turn further reduces the signal quality.

The depths of LFEs are consistent with that of a high resistivity zone, interpreted to be under high fluid pressure and facilitating brittle failure (Becken et al., 2011). The top of the LFE distribution is close to the bottom of a low velocity layer at $X = -2$ km, which also shows low V_p/V_s ratio. The low value of V_p/V_s may indicate high quartz content (Christensen, 1996). There is an obvious LFE gap beneath the 2004 Parkfield earthquake rupture patch (Shelly and Hardebeck, 2010). A low resistivity fluid channel that connects the high conductivity zone beneath the Rinconada fault and the SAF was imaged in a 3D

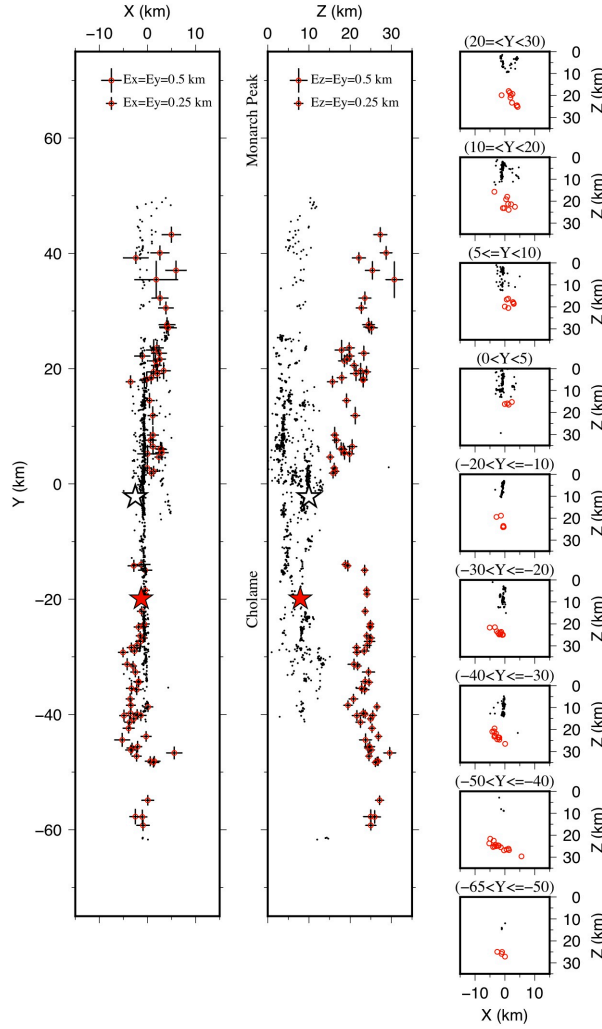


Figure 9. Maps and cross-sections showing LFE families' locations (red circles). The hypocenters of the 1966 and 2004 Parkfield earthquakes are shown in white and red stars, respectively. The black dots indicate regular earthquakes.

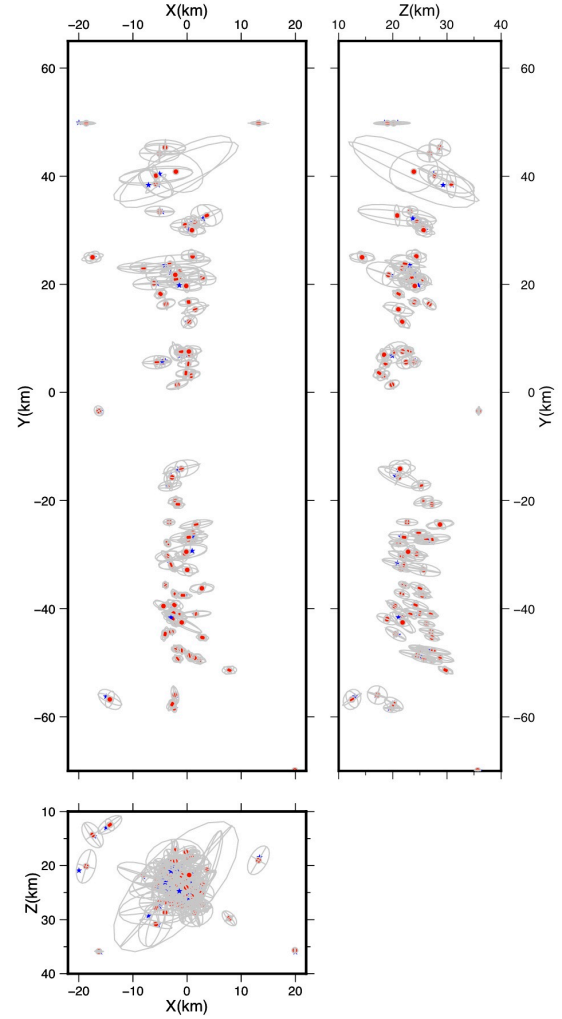


Figure 10. LFE family location results using the NonLinLoc algorithm. The 68% confidence ellipsoids are shown in gray. The blue stars denote maximum-likelihood hypocenters whereas the red dots denote maximum expectation hypocenters.

magnetotelluric inversion (Tietze and Ritter, 2013). They hypothesized that a fluid-filled porosity network causes fault weakening, so brittle failure as LFEs cannot occur. The V_p/V_s ratio in this region is higher than the surrounding area, also supporting high fluid content. An alternative hypothesis is that weak signals of undetected LFEs may be hidden by background noise (Shelly and Hardebeck, 2010).

Conclusions and future tomography work

New earthquake and LFE data have been employed to update an existing 3D V_p model and develop a new V_s model for the Parkfield region using double-difference tomography. A deep LVZ between the SAF and Rinconada fault was imaged in our inversion that is close to a high conductivity zone. Two other smaller LVZs in the lower crust are also present in the new model. Such LVZs may reflect fragments of metasedimentary rocks in the Parkfield region. The V_s model reveals several LVZs at shallow depth that are consistent with areas of high amplitude strong motion from the 2004 Parkfield earthquake. We also relocated 84 LFE families with the new model. The relocation results are generally consistent with the

previous study of Shelly and Hardebeck (2010); location uncertainties of most LFE families are less than 5 km.

Although more S picks were used in our inversion, the resolution of our Vs model is still not as good as the Vp model. An alternative choice is ambient noise tomography (ANT). ANT has been utilized in southern California (Shapiro et al., 2005; Zigone et al., 2015), a small region near Parkfield (Roux, 2009) and many other areas. The velocity contrast across the SAF was imaged by the previous ANT study (Roux, 2009), and a new body-wave and surface-wave joint inversion method applied to the same area revealed further small-scale features (Zhang et al., 2014). Application of ANT and joint tomography may be the keys to further improving our knowledge of the 3D Vs structure in the Parkfield region.

(2) Preliminary surface-wave dispersion analysis in the greater Parkfield region from ambient noise

In order to further constrain the S-wave structure in the Parkfield region, we have begun to explore the use of surface wave dispersion data from ambient noise, with the ultimate goal of joint body wave-surface wave inversion. The joint inversion of body wave arrival-time data and surface wave dispersion data for global and teleseismic 3-D Vp and Vs structure has been around in various forms for decades (Woodhouse and Dziewonski, 1984; Antolik et al., 2003; West et al., 2004), but it is a relatively new development for local earthquake tomography (Zhang et al., 2014; Syracuse et al., 2015). Refinements to this joint inversion methodology are continuing, for example replacing the standard two-step inversion of surface wave dispersion with a single step inversion (Fang et al., 2015). The surface-wave data typically provide denser spatial sampling than the body-wave data, since the paths connecting potentially all station pairs beyond a couple of wavelengths separation can be utilized, and the surface waves also have better resolution near the surface. We also find that in such joint inversions, it is often possible to reduce the applied smoothing regularization thanks to the additional constraints on the model provided by the two data types. This can lead to sharper models from the joint inversion that can actually fit the data better than the separate inversions. Determining the optimal data weighting and model smoothing parameters requires careful exploration, however, and checkerboard resolution tests need to be examined.

We have done some preliminary work to demonstrate that this goal is feasible. Figure 11 shows an example comparison of the use of standard linear stacking versus phase-weighted stacking (PWS) to generate noise correlation functions (NCFs). The use of PWS allows us to extract much higher quality NCFs. Figure 12 shows a sample record section of NCFs obtained using PWS, illustrating the quality of the results and the clear, varying moveout and dispersion that is evident. In particular, paths to stations on the southwest side of the SAF display noticeably higher apparent velocities than paths to stations on the northeast side. Modeling of group travel times at a period of 5 s with the fast marching surface-wave tomography (FMST) code of Rawlinson (rses.anu.edu.au/~nick/) yields the group velocity map in Figure 13. Such maps for a range of periods can be used to derive a 3D Vs model, and ultimately they can be combined with body-wave data in a joint inversion for 3D Vp and Vs structure (Zhang et al., 2014).

(3) LFE and NVT location

The other main effort undertaken with the support of this award is an investigation of the reliability of the envelope correlation method for locating NVT. The underlying question is whether the scattered locations of SAF NVT in studies such as Zhang et al. (2010) and Guilhem and Nadeau (2012) in contrast to the tightly clustered LFE locations such as in Shelly and Hardebeck (2010) is real. There is a debate as to whether there is a distinct difference in the sources of NVT versus LFEs, or if instead the scattered NVT locations are due to bias/artifacts in the envelope correlation method used to locate NVT. There is no direct way to answer this question. Instead, we develop a simulation strategy to determine whether the envelope correlation procedure applied to superimposed LFE seismograms leads to locations that "represent the centroid source location of nearly all of the NVT burst energy" (Guilhem and Nadeau, 2012). Our hypothesis is that seismograms consisting of superimposed LFEs occurring at different times and with varying amplitudes will yield locations from the envelope correlation method that are not the centroid of the superimposed LFEs, but rather are somewhat randomly scattered. If our hypothesis is

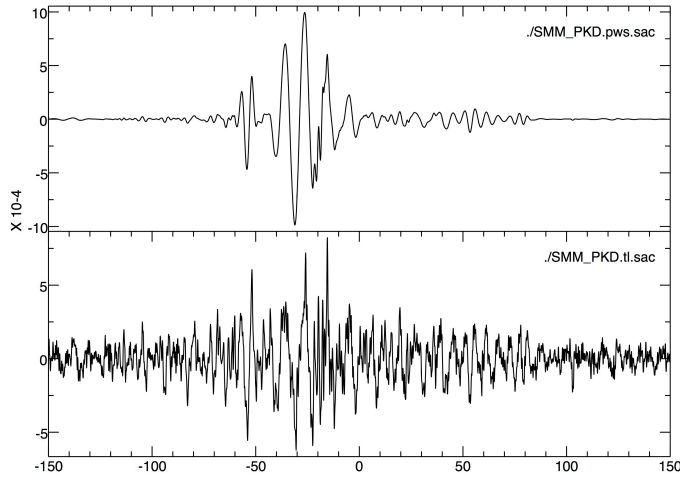


Figure 11. Comparison of noise correlation functions obtained from the station pair SMM and PKD. The top panel shows the result from using phase-weighted stacking and the bottom panel shows the results from standard linear stacking. Note the substantial high-frequency noise content of the linear stack relative to the phase-weighted stack. Note that both are strongly one-sided.

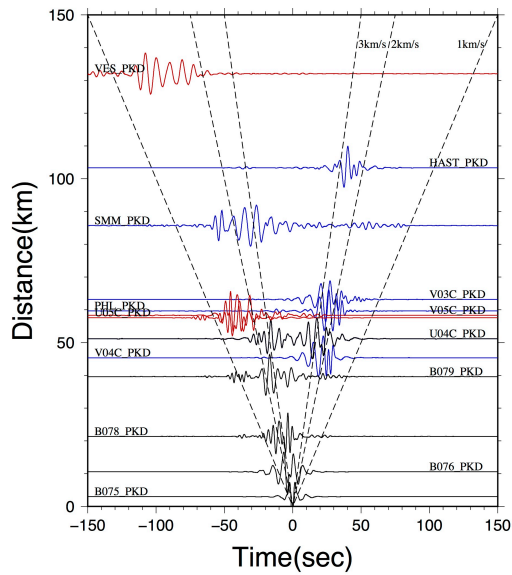


Figure 12. Record section of noise correlation functions between station PKD and broadband stations up to ~130 km separation. The dashed lines indicate moveouts of 3, 2, and 1 km/s. The noise correlation functions are largely one-sided due to the prevalent noise direction from the Pacific Ocean. Traces shown in black are for stations close to the SAF, whereas those in red are northeast of the SAF and those in blue are southwest of the SAF. As expected, the blue traces show higher apparent velocities, since sediments are generally thinner on the southwest side and the underlying granitic rocks have high S-wave velocity at relatively shallow depths.

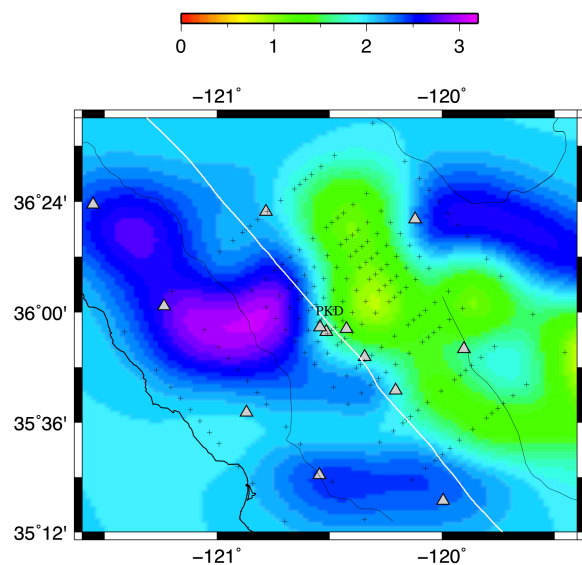


Figure 13. Preliminary Rayleigh wave group velocity map at 5 s period for the study region (in km/s). Triangles are the stations used that fall within the plot boundary, with station PKD shown for reference. Note the very strong group velocity contrast across the SAF (white line).

correct, that does not prove that NVT and LFEs are one and the same thing, but it would strongly call into question the validity of the broad volumetric distribution of NVT found by Nadeau and coworkers.

We have set up a procedure to test this hypothesis. Initially, we use a half-space velocity model (for simplicity) for computing travel times between LFE source locations (taken from Shelly and Hardebeck (2010)) and the HRSN stations used by Nadeau and coworkers for most of their NVT location work. Using a set of individual catalog LFE occurrence times (Shelly, pers. comm.), we use the travel times to superimpose the LFE waveforms (from our stacks) at appropriate arrival times for each HRSN station, with random noise added (Figure 14). The resulting waveforms are then processed and the locations are determined in the manner described in detail in the supplementary material of Nadeau and Guilhem (2009), using station-pair differential times. For reference, we also apply the same processing and location steps to the waveform stacks for individual LFEs.

Our initial results show that the relocation results for individual LFEs are rather poor, due to the heterogeneous nature of the LFE waveforms even for relatively nearby stations. For the simulated tremor events, the relocations are found to concentrate near the location of the first LFE in the simulated tremor event, not near the centroid of the suite of contributing LFEs. This combination of factors may be responsible for the scatter in the NVT locations based on envelope correlation. We will continue to test our hypothesis using additional tremor events with different catalog locations and involving different overlapping LFEs and varying superposition strategies, as well as using our 3D Vp and Vs models to calculate travel times and locate simulated tremor events.

We also collaborated with Rebecca Harrington and others on the examination of the spatial relationships between earthquakes and LFEs. In the Cholame area, the depth of the boundary between earthquakes and LFEs changes along strike, roughly following the 350° isotherm, and with a ~5 km separation between the two event types. There are significant clusters of LFEs near the 2004 Parkfield hypocenter and the northern boundary of the 1857 Fort Tejon rupture zone, suggesting the presence of frictional heterogeneities where larger earthquakes tend to nucleate.

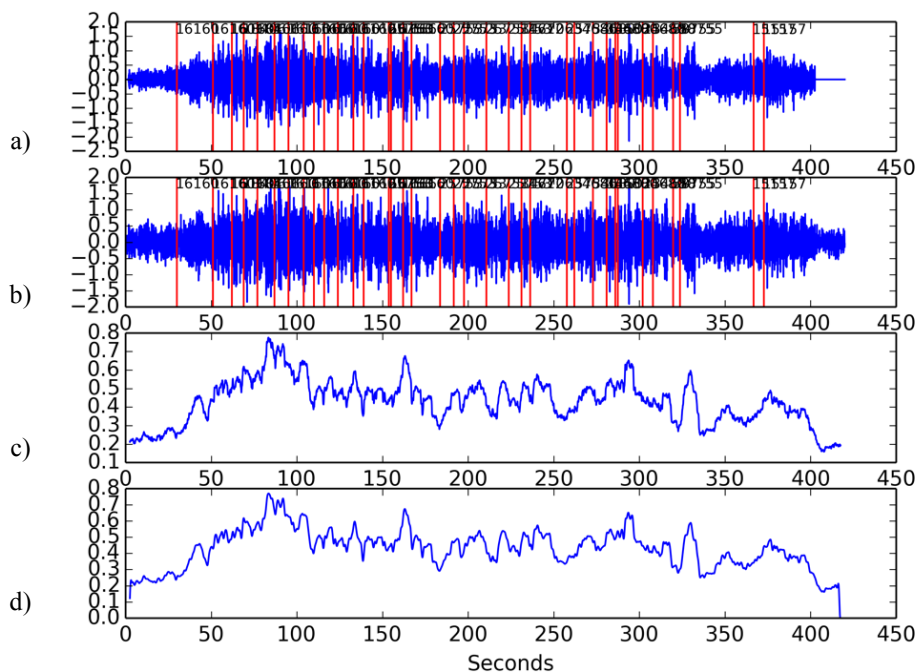


Figure 14. (a and b) Example of superimposing multiple LFEs and two levels of background noise to create simulated tremor. Red vertical lines show the arrival of sub-events. (c) RMS envelope time series for the simulated tremor seismograms in (b), and (d) the envelope time series in (c) smoothed with 0.07 Hz 2-pass low-pass filter.

References

- Antolik, M., Y. J. Gu, G. Ekstrom, and A. M. Dziewonski (2003), J362D28: A new joint model of compressional and shear velocity in the Earth's mantle, *Geophys. J. Int.*, 153, 443-466.
- Bakun, W. H. and Lindh, A. G. (1985), The Parkfield, California, earthquake prediction experiment, *Science*, 229(4714), 619-624.
- Becken, M., Ritter, O., Bedrosian, P. A., and Weckmann, U. (2011), Correlation between deep fluids, tremor and creep along the central San Andreas fault. *Nature*, 480(7375), 87-90.
- Bennington, N. L., C. Thurber, Z. Peng, H. Zhang, and P. Zhao (2013), Incorporating fault zone head wave and direct wave secondary arrival times into seismic tomography: Application at Parkfield, California, *J. Geophys. Res.*, 118, 1-7, doi:10.1002/jgrb.50072.
- Bleibinhaus, F., Hole, J. A., Ryberg, T., and Fuis, G. S. (2007), Structure of the California Coast Ranges and San Andreas Fault at SAFOD from seismic waveform inversion and reflection imaging. *J. Geophys. Res.*, 112, B06315.
- Brocher, T. (2005), Empirical relations between elastic wavespeeds and density in the Earth's crust. *Bull. Seismol. Soc. Am.*, 95(6), 2081-2092.
- Christensen, N. I. (1996), Poisson's ratio and crustal seismology, *J. Geophys. Res.*, 100, 9761-9788.
- Eberhart-Phillips, D. (1990), Three-dimensional P and S velocity structure in the Coalinga Region, California. *J. Geophys. Res.*, 95(B10), 15343-15363.
- Eberhart-Phillips, D. and A. J. Michael (1993), Three-dimensional velocity structure, seismicity, and fault structure in the Parkfield region, central California, *J. Geophys. Res.*, 98, 15,737-15,758.
- Fang, H., H. Yao, H. Zhang, Y.-C. Huang, and R. D. van der Hilst (2015), Direct inversion of surface wave dispersion for three-dimensional shallow crustal structure based on ray tracing: methodology and application, *Geophys. J. Int.*, 201, 1251-1263, doi:10.1093/gji/ggv080.
- Fletcher, J. B., and Baker, L. M. (2010), Analysis of nonvolcanic tremor on the San Andreas fault near Parkfield, CA using US Geological Survey Parkfield Seismic Array. *J. Geophys. Res.*, 115, B10305.
- Gallovic, F., Kaser, M., Burjanek, J. and Papaioannou C. (2010), Three-dimensional modeling of near-fault ground motions with nonplanar rupture models and topography: case of the 2004 Parkfield earthquake. *J. Geophys. Res.*, 115, B03308.
- Ghosh, A., J. E. Vidale, Z. Peng, K. C. Creager, and H. Houston (2009), Complex nonvolcanic tremor near Parkfield, California, triggered by the great 2004 Sumatra earthquake, *J. Geophys. Res.*, 114, B00A15, doi:10.1029/2008JB006062.
- Guilhem, A., and Nadeau, R. M. (2012), Episodic tremors and deep slow-slip events in Central California. *Earth and Planetary Science Letters*, 357, 1-10.
- Hardebeck, J. (2010), Seismotectonics and fault structure of the California central coast. *Bull. Seismol. Soc. Am.*, 100, 1031-1050.
- Hill, D.P., and S. Prejean (2013), Dynamic triggering, in H. Kanamori (ed.) *V. 4 Earthquake Seismology, Treatise on Geophysics*, 2nd edition (G. Schubert, ed. in chief), Elsevier, Amsterdam.
- Horstmann, T., Harrington, R. M., and Cochran, E. S. (2013), Semiautomated tremor detection using a combined cross-correlation and neural network approach. *J. Geophys. Res.*, 118(9), 4827-4846.
- Horstmann, T., Harrington, R. M. and Cochran, E. S. (2015), Using a modified time-reverse-imaging technique to locate low-frequency earthquakes on the San Andreas fault near Cholame, California, *Geophys. J. Int.*, 203, 1207-1226.
- Lin, G., Thurber, C. H., Zhang, H., et al. (2010), A California statewide three-dimensional seismic velocity model from both absolute and differential times. *Bull. Seismol. Soc. Am.*, 100(1), 225-240.
- Lomax, A., Michelini A., and Curtis A. (2009), Earthquake location, direct, global-search methods, in *Encyclopedia of Complexity and System Science*, Part 5, Meyers, R. A. (ed.), Springer, New York, pp. 2449-2473.
- McPhee, D. K., Jachens, R. C., and Wentworth, C. M. (2004), Crustal structure across the San Andreas Fault at the SAFOD site from potential field and geologic studies. *Geophys. Res. Lett.*, 31, L12S03.

- Michellini, A., and McEvilly, T. V. (1991), Seismological studies at Parkfield, I simultaneous inversion for velocity structure and hypocenters using cubic B-splines parameteriation. *Bull. Seismol. Soc. Am.*, 81, 524-522.
- Nadeau, R. M., and Dolenc, D. (2005), Nonvolcanic tremors deep beneath the San Andreas Fault. *Science*, 307(5708), 389-389.
- Nadeau, R. M., and Guilhem, A. (2009), Nonvolcanic tremor evolution and the San Simeon and Parkfield, California, earthquakes. *Science*, 325, 191-193.
- Ozacar, A. A., and Zandt, G. (2009), Crustal structure and seismic anisotropy near the San Andreas Fault at Parkfield, California. *Geophys. J. Int.*, 178, 1098-1104.
- Peng, Z., J. E. Vidale, A. G. Wech, R. M. Nadeau, and K. C. Creager (2009) Remote triggering of tremor along the San Andreas Fault in central California, *J. Geophys. Res.*, 114, B00A06, doi:10.1029.2008JB006049.
- Peng, Z., Vidale, J. E., Creager, K. C., Rubinstein, J. L., Gomberg, J., and Bodin, P. (2008), Strong tremor near Parkfield, CA, excited by the 2002 Denali Fault earthquake. *Geophys. Res. Lett.*, 35, L23305.
- Rawles C., and Thurber C. (2015), A nonparametric method for automatic determination of P-wave and S-wave arrival times: application to local microearthquakes. *Geophys. J. Int.*, 202(2), 1164-1179.
- Roux, P. (2009), Passive seismic imaging with directive ambient noise: application to surface waves and the San Andreas Fault in Parkfield, CA. *Geophys. J. Int.*, 179, 367-373.
- Ryberg, T., Haberland, C., Fuis, G. S., Ellsworth, W. L., and Shelly, D. R. (2010), Locating non-volcanic tremor along the San Andreas Fault using a multiple array source imaging technique. *Geophys. J. Int.*, 183, 1485-1500.
- Şeşetyan, K., E. Çaktı, and R. Madariaga, Engineering implications of source parameters and 3D wave propagation modeling for the 2004 Parkfield, California, earthquake. *Bull. Seismol. Soc. Am.*, 105, 1739-1755, doi: 10.1785/0120140261.
- Shakal, A., Haddadi, H., Graizer, V., Lin, K. and Huang M. (2006), Some key features of the strong-motion data from the M6.0 Parkfield, California, earthquake of 28 September 2004. *Bull. Seismol. Soc. Am.*, 96, S90-S118.
- Shapiro, N. M., Campillo, M., Stehly, L., and Ritzwoller, M. H. (2005), High-resolution surface-wave tomography from ambient seismic noise. *Science*, 307(5715), 1615-1618.
- Shelly, D. R. (2009), Possible deep fault slip preceding the 2004 Parkfield earthquake, inferred from detailed observations of tectonic tremor, *Geophys. Res. Lett.*, 36, L17318, doi:10.1029/2009GL039589.
- Shelly, D. R. (2015), Complexity of the deep San Andreas Fault zone defined by cascading tremor, *Nature Geoscience*, 8, 145-151, doi:10.1038/ngeo2335.
- Shelly, D. R., W. L. Ellsworth, T. Ryberg, C. Haberland, G. S. Fuis, J. Murphy, R. M. Nadeau, and R. Bürgmann (2009), Precise location of San Andreas Fault tremors near Cholame, California, using seismometer clusters: Slip on the deep extension of the fault?, *Geophys. Res. Lett.*, 36, L01303, doi:10.1029/2008GL036367.
- Shelly, D. R., and Hardebeck, J. L. (2010), Precise tremor source locations and amplitude variations along the lower-crustal central San Andreas Fault. *Geophys. Res. Lett.*, 37, L14301.
- Snyder, D. B., and Carr, W. J. (1984), Interpretation of gravity data in a complex volcano-tectonic setting, southwestern Nevada. *J. Geophys. Res.*, 89(B12), 10193-10206.
- Syracuse, E., M. Maceira, H. Zhang, and C. Thurber (2015), Seismicity and structure of Akutan and Makushin Volcanoes, Alaska, using joint body- and surface-wave tomography, *J. Geophys. Res.*, 120, doi:10.1002/2014JB011616.
- Thomas, A. M., R. Bürgmann, D. R. Shelly, N. M. Beeler, and M. L. Rudolph (2012), Tidal triggering of low frequency earthquakes near Parkfield, California: Implications for fault mechanics within the brittle-ductile transition, *J. Geophys. Res.*, 117, B05301, doi:10.1029/2011JB009036.
- Thomas, A. M., R. M. Nadeau, and R. Bürgmann (2009), Tremor-tide correlations and near-lithostatic pore pressure on the deep San Andreas fault, *Nature*, 462, 1048–1051, doi:10.1038/nature08654.

- Thurber, C., T. Brocher, H. Zhang, and V. Langenheim (2007), Three-dimensional P-wave velocity model for the San Francisco Bay region, California, *J. Geophys. Res.*, 112, B07313, doi:10.1029/2006JB004682.
- Thurber, C. H., Roecker, K., Gold, M., Powell, L. and Rittger, K. (2003), Earthquake locations and three-dimensional fault zone structure along the creeping section of the San Andreas fault near Parkfield, CA: Preparing for SAFOD. *Geophys. Res. Lett.*, 30(3), 1112.
- Thurber, C. H., Zeng, X., Thomas, A. M., and Audet, P. (2014), Phase-weighted stacking applied to low-frequency earthquakes. *Bull. Seismol. Soc. Am.*, 104(5), 2567-2572.
- Thurber, C., Zhang, H., Brocher, T., and Langenheim, V. (2009), Regional three-dimensional seismic velocity model of the crust and uppermost mantle of northern California. *J. Geophys. Res.*, 114, B01304.
- Thurber, C., H. Zhang, F. Waldhauser, J. Hardebeck, A. Michael, and D. Eberhart-Phillips (2006), Three-dimensional compressional wavespeed model, earthquake relocations, and focal mechanisms for the Parkfield, California, region, *Bull. Seismol. Soc. Am.*, 96, S38-S49.
- Tietze, K., and Ritter, O. (2013), Three-dimensional magnetotelluric inversion in practice—the electrical conductivity structure of the San Andreas Fault in Central California. *Geophys. J. Int.*, 195(1), 130-147.
- Trehu, A. M., and Wheeler, W. H. (1987), Possible evidence for subducted sedimentary materials beneath central California, *Geology*, 15, 254-258.
- West, M., W. Gao, and S. Grand (2004), A simple approach to the joint inversion of seismic body and surface waves applied to the southwest U.S., *Geophys. Res. Lett.*, 31, L15615, doi:10.1029/2004GL020373.
- Woodhouse, J. H., and A. M. Dziewonski (1984), Mapping the upper mantle: Three-dimensional modeling of Earth structure by inversion of seismic waveforms, *J. Geophys. Res.*, 89, 5953-5986.
- Zhang, H., Nadeau, R. M., and Toksoz, M. N. (2010), Locating nonvolcanic tremors beneath the San Andreas fault using a station-pair double-difference location method, *Geophys. Res. Lett.*, 37, L13304.
- Zhang, H., and Thurber, C. H. (2003), Double-difference tomography: The method and its application to the Hayward fault, California, *Bull. Seismol. Soc. Am.*, 93, 1875-1889.
- Zhang, H., and Thurber, C. (2006), Development and applications of double-difference seismic tomography, *Pure and Applied Geophysics*, 163, 373-403.
- Zhang, H., Thurber, C., and Bedrosian, P. (2009), Joint inversion for V_p , V_s , and V_p/V_s at SAFOD, Parkfield, California, *Geochemistry, Geophysics, Geosystems*, 10, Q11002.
- Zhang, H., Maceira, M., Roux, P., and Thurber, C. (2014), Joint inversion of body-wave arrival times and surface-wave dispersion for three-dimensional seismic structure around SAFOD, *Pure and Applied Geophysics*, 171, 3013-3022.
- Zigone, D., Ben-Zion, Y., Campillo, M., and Roux P. (2015) Seismic tomography of the Southern California plate boundary region from noise-based Rayleigh and Love waves, *Pure and Applied Geophysics*, 172, 1007-1032.

Bibliography of published work

Journal publications

- Harrington, R. M., E. S. Cochran, E. M. Griffiths, X. Zeng, C. Thurber, and D. R. Shelly (2016), Earthquake relocations along the San Andreas Fault near Cholame, California suggest along-strike variations in fault frictional properties, Bull. Seism. Soc. Am., 106, doi: 10.1785/0120150171.
- Zeng, X., C. H. Thurber, D. R. Shelly, R. M. Harrington, E. S. Cochran, N. L. Bennington, D. E. Peterson, B. Guo, and K. McClement, Three-dimensional P- and S-wave velocity structure and low-frequency earthquake locations in the Parkfield, California region, Geophys. J. Int., in revision.

Meeting presentations

- Griffiths, E., R. Harrington, E. Cochran, X. Zeng, and C. Thurber (2015), Earthquake relocations along the San Andreas Fault provide insight into rupture processes at intermediate depths, 2015 Joint Assembly, Montreal, Canada, abstract S34B-0307.
- Zeng, X., C. H. Thurber, D. R. Shelly, N. L. Bennington, E. S. Cochran, and R. M. Harrington, 3D P and S wave velocity structure and tremor locations in the Parkfield region, abstract S23C-4545, Fall AGU meeting, 2014.
- Zhang, H., and C. Thurber, Double-difference seismic tomography: Multiple scales and joint inversions, Annual Meeting of the Seismological Society of America, Pasadena, CA, April 2015.